Materials Advances

ROYAL SOCIETY OF CHEMISTRY

PAPER

View Article Online
View Journal | View Issue

Cite this: *Mater. Adv.*, 2025, 6, 6305

Doping of steel slag waste as a sustainable filler in ceramic tile composites for enhanced gamma-ray shielding

Rehab M. El-Sharkawy, *[a] Meshari Almeshari,[b] Yasser Alzamil,[b] Ahmad Abanomy,[c] Bader Alshoumr,[d] Asmaa M. Halbas,[e] Elhassan A. Allam,[f] Mohamed E. Mahmoud,[f] H. A. Saudi[g] and Atef El-Taher[h]

Received 29th March 2025,
Accepted 22nd July 2025

DOI: 10.1039/d5ma00287g

rsc.li/materials-advances

This study explores the incorporation of electric arc furnace (EAF) steel slag, a common industrial by-product, as a sustainable filler in ceramic tile composites for enhanced gamma-ray shielding. Ceramic tile samples were prepared by varying the EAF slag contents (0–40 wt%) and characterized using FT-IR, XRD, SEM, and EDX. Mechanical properties, including modulus of rupture (MOR) and Vickers microhardness (H_v), were evaluated. The sample with 20 wt% slag exhibited the highest MOR (14.0 ± 0.21 MPa), while H_v values increased with slag content. Gamma-ray shielding parameters, such as mass attenuation coefficient (μ_m), effective atomic number (Z_{eff}), effective electron density (N_{el}), and half-value layer (HVL), were measured by a NaI(Tl) detector at a photon energy range from 238 to 2614 keV. The sample with 40 wt% slag (CT-EAF-4) demonstrated the best shielding performance, with a μ_m of 0.1811 $cm^2\ g^{-1}$, Z_{eff} of 7.312, N_{el} of 0.2813 × 10^{23} electrons g^{-1}, and the lowest HVL (0.253 cm) at 238 keV. These findings highlight the effectiveness of EAF slag as an eco-friendly additive for enhancing both the mechanical and radiation shielding properties of ceramic tiles. Consequently, this approach provides a sustainable solution for the reuse of industrial waste in the development of protective building materials.

1. Introduction

The application of high-energy ionizing radiation has become prevalent in numerous advanced technological fields, such as medical diagnostics and therapy,[1] elemental analysis through the non-destructive photoactivation analysis (PAA) technique,[2] irradiation response testing of metal–oxide–semiconductor (MOS) capacitors,[3] food processing,[4] and various forms of diagnostic imaging.[5,6] The implementation of these advanced technologies presents numerous risks, especially for those exposed to radiation. Such exposure can pose significant physical damage as a result of the potential effects of dangerous rays emitted. Prolonged radiation exposure can lead to severe consequences for living tissues, including radiation sickness, cancer, genetic mutations, and, in extreme cases, mortality.[7] Consequently, adopting appropriate measures to minimize radiation exposure has consistently been a critical concern. This is especially important for protecting both employees and patients in hospitals, particularly within nuclear medicine and medical research facilities. As a result, there is increasing emphasis on the development of radiation shielding materials to mitigate the biological effects associated with such radiation.[8,9] Over the past few decades, numerous materials containing elements with high atomic weight (Z) have been employed for this purpose, including steel, glass, clay, lead, marble, granite, polymers, and concrete.[10–15] The effectiveness of these shielding materials is determined by their density and mass, which results in the selection of dense and heavy shields. There is a growing interest in the application of composite materials within radiation shielding studies, primarily owing to their versatile and adjustable structural attributes.[16–18] Nonetheless, there remains significant demand for advanced heat-transfer shielding materials that optimize both size efficiency and affordability. These materials must also ensure structural

[a] *Chemistry Department, Faculty of Dentistry, Pharos University in Alexandria, P.O. Box 37, Sidi Gaber, Alexandria, Egypt. E-mail: rehab.mansour@pua.edu.eg; Tel: +002-01229727752*
[b] *Department of Diagnostic Radiology, College of Applied Medical Sciences, University of Hail, Hail, Saudi Arabia*
[c] *Department of Radiological Sciences, College of Applied Medical Sciences, King Saud University, P.O. Box 10219, Riyadh 11433, Saudi Arabia*
[d] *Department of Health Informatics, College of Public Health and Health Informatics, University of Hail, Hail, Saudi Arabia*
[e] *Chemistry Department, Faculty of Science, Alexandria University, P.O. Box 426, Ibrahimia 21321, Alexandria, Egypt*
[f] *Lecico Company for Ceramic Industry, Alexandria, Egypt*
[g] *Physics Department, Faculty of Science, Al-Azhar University (Females Branch), Cairo, Egypt*
[h] *Physics Department, Faculty of Science, Al-Azhar University, Assiut 71452, Egypt*

durability and provide reliable shielding performance for the safe handling and storage of radioactive materials.

Ceramic tile is among the most widely used materials in the construction sector and has been extensively developed to fulfill industry requirements. The tile composition represents a ternary system comprising silica (10–30 wt%), clay (30–60 wt%), and feldspar (10–60 wt%).[19] The fundamental base material for ceramic tiles is clay, while silica is utilized as a filler to minimize shrinkage. Feldspar is also introduced as a fluxing agent, which significantly lowers the firing temperature during the process.[20,21] Ceramic materials are increasingly recognized for their effectiveness in gamma-radiation protection, especially in the development of fusion and fission reactors and the management of radioactive waste. This is attributed to their high melting point, which exceeds 1200 °C. In addition, they exhibit a combination of desirable properties, including high strength and hardness, excellent insulating performance, low thermal expansion, low dielectric constants, strong resistance to oxidation, and environmentally friendly characteristics. Mahmoud *et al.*[22] analyzed the mechanical, physical, as well as gamma-ray shielding properties of standard ceramic tiles incorporated with different weight fractions of micro-sized lead oxide (PbO), specifically at 2.5%, 5%, 7.5%, and 10%. Oto *et al.*[23] examined the shielding capabilities of ceramic specimens infused with multiple proportions of Mo (molybdenum), namely 5%, 10%, 20%, and 30%, against fast neutrons and gamma-rays. Akman *et al.*[24] performed a comprehensive assessment of gamma-ray shielding parameters, including μ_m, N_{el}, Z_{eff}, MFP (mean free path), and HVL, across six distinct ceramic specimens to evaluate their radiation shielding capabilities. In another study, Singh *et al.*[25] calculated the gamma energy buildup factor (EBF) and assessed the fast neutron cross section across various ceramic matrices. The study by Kacal *et al.*[26] evaluated the shielding effectiveness of several ceramic samples against photons and fast neutrons. The study carried out by Jawad *et al.*[27] focused on determining the linear attenuation coefficient (μ) across various ceramic waste samples, using a gamma-ray spectrometer along with two radioactive sources, namely ^{60}Co and ^{137}Cs. Meanwhile, Ripin *et al.*[28] explored the X-ray shielding properties of ceramics composed of mullite and barite. Özdemir and Yılmaz[29] evaluated the neutron shielding effectiveness of flexible ceramic rubber composites.

Industrial activities result in the generation of substantial solid waste materials. The buildup of these materials is regarded as a primary contributor to environmental pollution.[30] There have been significant concerns regarding the handling and disposal of these materials. One effective solution to this issue is the recycling of solid waste by incorporating it into alternative raw materials. For instance, reusing by-products from industries can decrease the demand for natural resources in multiple productive sectors.[31] Research concerning the environmental impacts of solid waste recycling has gained significant importance over the past decade.[32–34] Numerous investigations have addressed the incorporation of industrial wastes in ceramic tile production, including fly ash, waste glass, and slags derived from blast furnaces and electric arc furnaces (EAF).[35–37]

In the iron and steel production industry, EAF slag is identified as one of the most prevalent by-products generated. Typically, the process of manufacturing one ton of steel results in approximately 200 kg of EAF slag, while the blast furnace method yields around 400 kg of by-products.[32] The primary chemical components of EAF slag include calcium and iron oxides, along with aluminum oxide (Al_2O_3), magnesium oxide (MgO), and silicon dioxide (SiO_2). Additionally, it contains minor amounts of manganese oxide (MnO), chromium oxide (Cr_2O_3), titanium dioxide (TiO_2), sodium oxide (Na_2O), and potassium oxide (K_2O).[36] The stable crystalline structure, high contents of magnetite and hematite, make EAF slag suitable for use in construction materials like cement, aggregates, and bricks.[36,38–40] Previous investigations have revealed that EAF slag can serve as a fluxing agent similar to feldspar in manufacturing ceramic tiles.[36,41,42] This incorporation results in improved density, reduced porosity and water absorption, as well as enhanced mechanical strength.[43] Additionally, EAF slag has been demonstrated to effectively enhance gamma-ray shielding performance in concrete, making it a viable alternative to conventional aggregates fillers.[44–47]

The objective of this study is to bridge the knowledge gap regarding the correlation between gamma-ray shielding efficiency and the structural, physical, and mechanical properties of ceramic tiles that incorporate varying ratios of EAF slag, particularly 10.0 wt%, 20.0 wt%, 30.0 wt%, and 40.0 wt%. While previous studies have explored the use of EAF slag in ceramic matrices primarily as a flux or aggregate, the current investigation is distinct in several key aspects. Specifically, quartz was partially replaced by a high FeO-content EAF slag in the clay matrix to enhance densification and glass phase formation during firing. This novel compositional adjustment can optimize both mechanical strength and effectiveness in radiation shielding when compared to prior reports. Additionally, this study offers a comprehensive multifunctional evaluation by correlating structural (XRD, FTIR, SEM), mechanical (MOR, H_v), physical (water absorption, density), and gamma-ray shielding properties (mass attenuation coefficient, half-value layer, effective atomic number, electron density). Such a holistic characterization approach is rarely found in previous works. Moreover, the developed ceramic tiles in this work were fabricated using a green process without requiring additional binders, sintering aids, or thermal treatments. This supports process scalability and aligns with current manufacturing infrastructure, offering a more practical route for adoption. These distinctions collectively highlight the practical and scientific significance of advancing the development of sustainable, multifunctional, and industrially viable radiation-shielding ceramic composites for critical applications in military shielding, radiotherapy units, advanced equipment protection, and radioactive waste management.

2. Experimental details

2.1. Materials used

The EAF slag, classified as solid waste, was collected from the Ezz Steel production plant in Egypt. This material is produced

Table 1 Chemical composition (%) of raw EAF steel slag sample

Component[a]	%
FeO	82.3
Metal Fe	5.7
SiO_2	3.2
CaO	3.1
MgO	2.7
Al_2O_3	1.4
MnO	0.5
P_2O_5	0.1
S	0.01
K_2O	0.5
TiO_2	0.2
Cr_2O_3	0.3

[a] Chemical composition of slag provided by the steelmaking company.

as a by-product during the initial phase of steel production, wherein pig iron, scrap metal, and calcium oxide are melted in an electric arc furnace. The density of the obtained EAF slag is less than that of molten steel, which allows the red-hot EAF slag to rise to the surface, where it is subsequently collected and solidified into a rock-like form. During the iron ore sizing process, fines of EAF slag were produced with particle sizes ranging from 3 to 5 mm, which were further processed to nanoscale dimensions using a ball mill. Table 1 lists the chemical composition of the EAF slag powder provided by the steelmaking company. The raw materials for the ceramic tiles utilized in the experimental studies include Aswanly clay ($Al_2Si_2O_5(OH)_4$ at 61.0%), calcite ($CaCO_3$ at 14.0%), feldspar ($KAlSi_3O_8$ at 12.4%), crushed recycled ceramic tiles (9.2%), and quartz (SiO_2 at 3.4%), all sourced from local suppliers.

2.2. Instrumentation

In the course of this investigation, multiple characterization techniques were utilized to assess the structural characteristics of the designed ceramic tile/EAF slag samples. The techniques employed included X-ray diffraction (XRD), scanning electron microscopy (SEM), energy dispersive X-ray (EDX), and Fourier transform infrared spectroscopy (FT-IR). Detailed specifications of these instruments are provided in Table 2.

The μ_m values, expressed in $cm^2\ g^{-1}$, of the EAF slag/ceramic tile composites were determined by measuring the transmission of gamma-rays through samples with six different thicknesses (Fig. 1). A sodium iodide scintillation detector, thallium-doped and identified by model number 802 from Canberra U.S.A., was used to recognize both the incident beams and the beams that were transmitted. The dimensions of this detector are 2×2 inches, and it features an energy resolution of 12.5% at 662 keV. The spectra collected were analyzed through the use of Canberra's Genie 2000 program. For energy calibration prior to testing, radioactive point sources including ^{137}Cs, ^{60}Co, and ^{232}Th, each with an activity of 10 Ci, were utilized. These sources were also employed as gamma-ray emitters during the tests. In order to establish the experiment, the samples under investigation were arranged in alignment with the collimated gamma-rays originating from the aforementioned radioactive sources. The determination of μ_m of the tested composite samples was conducted using Lambert's law.[16,17] This involved taking measurements in the presence and absence of the samples, repeated three times over different live times. The counting intervals were selected to ensure a minimum of ten thousand counts, thereby reducing the statistical uncertainties of the areas of net peak to less than or equal to 1.0%. The analysis of the theoretical μ_m values for the produced ceramic tile/EAF slag samples was conducted using the WINXCom program (version 3.1), which was developed by NIST.[25]

The evaluation of bulk densities (ρ) and AW% of the tested ceramic tile/EAF materials was conducted at 25 °C, following Archimedes' method as specified in ASTM C373-88.[48] The MOR measurement for the developed ceramic tile/EAF samples was carried out using a digital anti-fold universal testing instrument model HYK-10000A sourced from Shandong in China.[22] This instrument operates on a three-point bending system, adhering to the MS ISO 10545-4 and ASTM C-689-71 testing standards.[49] In order to verify the reliability of the measurements, five specimens were fabricated for each type of ceramic tile, followed by the calculation of the average values. The assessment of surface irregularities and curvature on the prepared ceramic tile/EAF composites was performed following the ISO 13006 testing method.[50] The measurements were captured using a dial gauge that offers a precision of 0.01 mm.

Hardness is characterized by the ratio of the test force exerted to the expected area of the resulting deliberate imprint. The determination of Vickers hardness (H_v) was conducted using a micro-hardness tester model Leco AMH 100 from the

Table 2 Instruments and their specifications

Instrument name	Model	Data	Conditions	Technique
Fourier-transform infrared spectrophotometer (FT-IR)	FTIR-3400s SHIMADZU	FT-IR spectrum	400–4500 cm^{-1}	Using KBr pellets
X-ray diffraction (XRD)	SHIMADZU lab x 6100, Kyoto, Japan	XRD spectrum	40 kV, 30 mA, λ = 1 Å, 2θ from 10 to 80, recording steps of the diffraction data of 0.02° at a time of 0.6 s, at room temperature (25 °C)	X-ray diffractometer, using target Cu-Kα
Scanning electron microscope (SEM)	JSM-6360LA, JEOL Ltd	SEM images	Imaging mode	Sputtering coating (JEOL-JFC-1100E)
Energy dispersive X-ray (EDX)	JSM-lT200, JEOL Ltd	EDX spectrum	Acceleration voltage 20.00 kV, WD 10.00 mm, Live time 30.00, high vacuum mode.	Energy dispersive X-ray

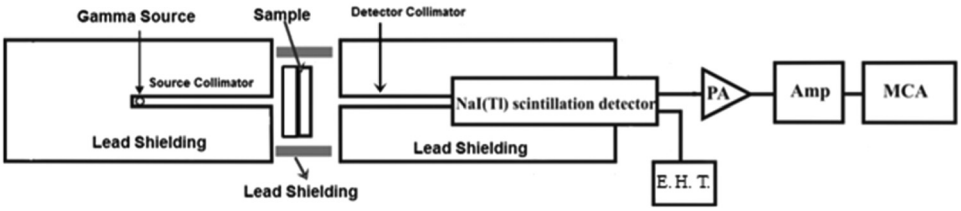

Fig. 1 Narrow beam experimental setup.

U.S.A. to perform sample indentation. The following formula can be applied to compute micro-hardness:[50]

$$H_v = 1.842p/d^2 \quad (1)$$

Here, p denotes the load applied during indentation, and d refers to the diagonal length of the resulting imprint.

2.3. Manufacturing of ceramic tile/EAF slag samples

In experimental studies, the fired ceramic tiles are generally made up of Aswanly clay (61.0%), calcite (14.0%), quartz (3.4%), feldspar (12.4%), along with 9.2% by weight of recycled and crushed ceramic tiles. The process of producing ceramic tiles is divided into two main stages: the formation of green bodies and the subsequent firing process. Before the green bodies are formed, the raw materials for standard reference ceramic bodies are proportioned gravimetrically, with careful attention paid to their moisture content. Following the weighing process, the pre-crushed materials are subjected to milling in a planetary ball mill. To achieve a more uniform sample, water is incorporated during this process. The grinding media employed is Alubit pebble, characterized by a composition of 92% alumina. Subsequently, varying proportions of powdered EAF slag, specifically 0.0% (control), 10.0%, 20.0%, 30.0%, and 40.0% by weight, were introduced into the raw materials of the standard reference ceramic bodies. It is essential to highlight that in the process of manufacturing the tile samples, the overall proportions of feldspar and clay were preserved; however, a portion of the quartz in the mixture was substituted with EAF slag. The composite was suspended using around 35% water, leading to a final slip residue that measured between 2% and 4%. The drying of the slip was performed through a process that included dry grinding of a cake with a hammer. Subsequently, the ground material was transferred to a mortar and passed through a 2 mm sieve to ensure uniform granule formation. This step was completed by carefully adding water to the powder, achieving an average moisture content of approximately 5–7%. The powder was then molded and inserted into a frame, where it underwent compression using a single-stroke hydraulic press with dimensions of 15 cm height, 20 cm width, and 0.8 cm thickness. A pressure of approximately 250 bar was applied for 20 min, facilitating the effective compaction of the sample into a rectangular tile. The green bodies, which had been pressed, were subjected to drying in a vertical dryer. The process commenced at a heating temperature of 110 °C for a period of 24 h. Subsequently, the temperature was raised to 150 °C for a duration of one to two hours, depending on the moisture content of the greenware. Ensuring that the residual moisture content remained below 1.0% was crucial to prevent the formation of fissures throughout the firing process. The final stage in the process involved the firing of ceramic bodies within a roller hearth kiln, which is characterized by a firing zone measuring 1.52 meters in length. This operation was carried out at a temperature of 1100 °C, with a heating rate set at 10 °C min^{-1}. Each firing cycle lasted 60 min, followed by a controlled cooling phase that lowered the temperature to 25 °C at a rate of 5 °C min^{-1}. As a result, standard rectangular fired ceramic bodies were produced. The temperature during firing was regularly established at a threshold lower than 1200 °C to avoid the melting of the EAF slag.[36] To determine the gamma-ray attenuation capabilities of each ceramic tile produced, standard specimens were prepared in the form of six discs, each measuring 0.80 cm in thickness and 2.5 cm in diameter. The chemical composition, density, and sample codes of the developed ceramic tile/EAF composite materials are presented in Table 3.

Table 3 Sample code, chemical composition (wt%), and bulk density (ρ) of the prepared ceramic tiles/EAF slag samples

Samples code	Composition (wt%)		Density (g cm^{-3})
	Ceramic tile	EAF slag	
CT-EAF-0	100.0	0.0	2.09 ± 0.75
CT-EAF-1	90.0	10.0	2.20 ± 0.68
CT-EAF-2	80.0	20.0	2.31 ± 0.95
CT-EAF-3	70.0	30.0	2.45 ± 0.49
CT-EAF-4	60.0	40.0	2.59 ± 0.77

3. Results and discussion

3.1. Structural characterization

3.1.1. FT-IR spectroscopy. The FT-IR spectra shown in Fig. 2a–d represent a typical ceramic tile, EAF slag, a ceramic tile incorporating 10.0 wt% EAF, and a ceramic tile incorporating 40.0 wt% EAF. These spectra are encompassed within the frequency spectrum of 400 to 4500 cm^{-1}. In Fig. 2a, the spectrum of the clay mixture used in the preparation of ceramic tile is shown, with no EAF slag addition. The peaks identified at 3690 and 1632 cm^{-1} correspond to the –OH vibration of water that is absorbed physically on the surface of the clay powder mixture.[17] Alternatively, the weak bands recorded at 3630 and 3455 cm^{-1} might be linked to the stretching vibration mode of the interlayer –OH.[22] Two additional peaks are observed, one located at 2517 cm^{-1} and the other at 2351 cm^{-1}, both attributed to the saturated C–H group and its associated

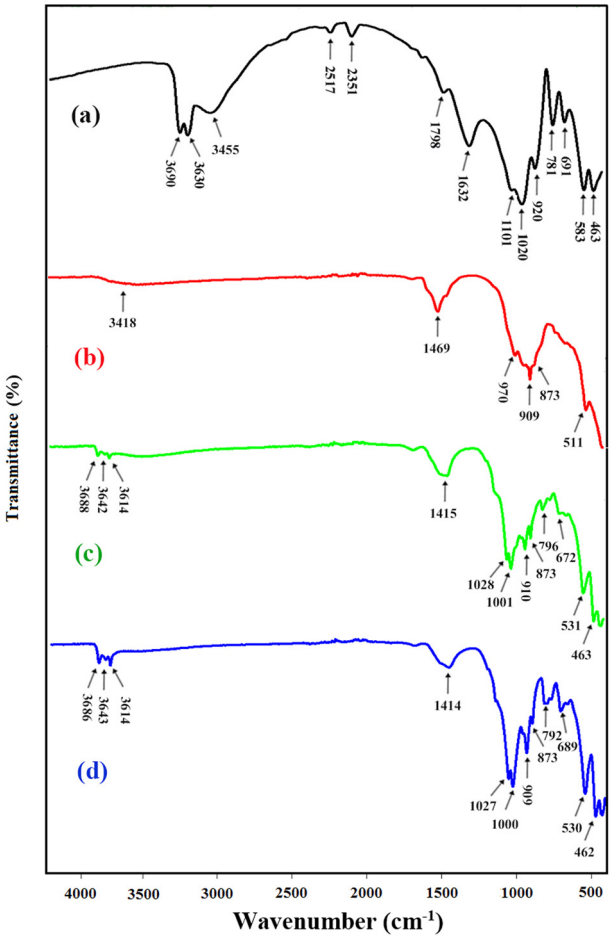

Fig. 2 FT-IR spectra of (a) standard ceramic tile, (b) electric arc furnace (EAF) steel slag, (c) ceramic tile including 10.0 wt% EAF, and (d) ceramic tile including 40.0 wt% EAF.

stretching vibrations.[51] Moreover, the medium bands observed at 781 and 583 cm^{-1} can be attributed to Si–O–Al stretching vibrations. On the other hand, the bands at 1020 and 463 cm^{-1} are likely due to Si–O vibrations that occur in the clay mixture in the tile matrix.[22] The peaks identified at 1101 and 920 cm^{-1} correspond to the vibrations of Fe–OH.[51] In addition, the weak band observed at 691 cm^{-1} may be associated with Mg–Al–OH vibrational modes, while the peak at 1798 cm^{-1} is attributed to Ca–O stretching vibrations.[22,51]

The EAF slag exhibits distinct FT-IR bands at 3418, 1469, 970, 909, 873, and 511 cm^{-1}, as illustrated in Fig. 2b. The peak observed at 3432 cm^{-1} is linked to the stretching vibration of hydroxyl groups, which arises from the presence of weakly adsorbed water molecules on the slag surface.[22] The notable bands identified at 873 and 1469 cm^{-1} correspond to the asymmetric bending and the stretching vibration modes of the carbonate group, respectively.[52] The presence of a band at 909 cm^{-1} is associated with the O–Si–O asymmetric stretching vibration, whereas the notable peak at 970 cm^{-1} is linked to the asymmetric stretching vibration of Si–O–Si.[52] It is notable that the weak band observed at 511 cm^{-1} is most likely due to the stretching vibrations of metal–oxygen bonds, including Si–O, Fe–O, Ca–O, and Mg–O. This observation reflects the significant mineral phases present in the EAF slag.[52]

The FT-IR spectra of ceramic tile/EAF slag samples (Fig. 2c and d) exhibit characteristic peaks corresponding to the clay mixture present in the ceramic tile matrix, in addition to typical vibrational bands attributed to the EAF slag. These findings confirm the effective integration of EAF slag into the ceramic tile structure.

3.1.2. X-ray diffraction (XRD). The XRD patterns presented in Fig. 3a–d correspond to the ceramic tile, EAF slag, alongside ceramic tiles, which incorporate 10.0 wt% and 40.0 wt% EAF slag. The XRD pattern of the tile clay mixture without the EAF slag (Fig. 3a) indicates the presence of both crystalline and amorphous phases. The sample is predominantly crystalline, reflecting the presence of minerals, such as quartz (SiO_2), calcite ($CaCO_3$), kaolinite ($Al_2Si_2O_5(OH)_4$), feldspar ($KAlSi_3O_8$), and other carbonate minerals. Meanwhile, the minor components present in the amorphous phase are attributed to hematite (Fe_2O_3).[51] The examination of the XRD patterns of the tile confirms that the clay mixture within the ceramic matrix is predominantly composed of feldspar, calcite, and kaolinite. Additionally, trace quantities of hematite and quartz have been detected.

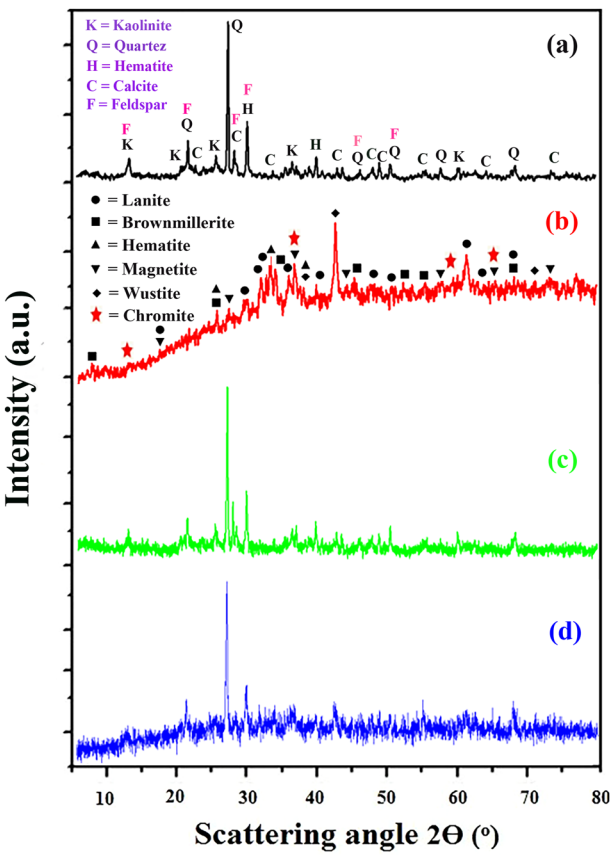

Fig. 3 XRD patterns of (a) standard ceramic tile, (b) electric arc furnace (EAF) steel slag, (c) ceramic tile including 10.0 wt% EAF, and (d) ceramic tile including 40.0 wt% EAF.

Fig. 3b illustrates the X-ray diffraction (XRD) pattern as well as the identification of crystalline phases present in the EAF slag sample. The analysis indicates that the predominant crystalline phases include Brownmillerite ($Ca_2(Al,Fe)_2O_5$) and Larnite (Ca_2SiO_4). Additionally, various iron oxides were identified, notably in the mineralogical forms of magnetite (Fe_3O_4), hematite (Fe_2O_3), magnesiochromite ($MgCr_2O_4$), wustite (FeO), and iron chromite ($FeCr_2O_4$). These findings are consistent with the earlier studies.[53] It is commonly observed that Fe^{2+} is partially substituted by Mg^{2+}, resulting in the presence of chromium-bearing phases, such as $MgCr_2O_4$ and $FeCr_2O_4$, in the diffractogram. These phases are collectively identified as chromite [$(Fe,Mg)Cr_2O_4$].[54] These observations align with the chemical composition (%) of the raw EAF slag, as presented in Table 1, which confirms the substantial presence of iron. It is important to note that, according to the data illustrated in Table 1, the EAF slag sample contains trace amounts of heavy metals that may be harmful to the environment. However, previous studies have demonstrated that incorporating it into ceramic matrices significantly reduces leachability. This effect is attributed to chemical immobilization and vitrification occurring during sintering.[31,32,35,36] Additionally, the concentrations of heavy metals (*e.g.*, Cr, Mn, Mg, Ti) in the analyzed EAF slag sample were found to be within the permissible limits established by USEPA, WHO, and local environmental regulations.[55]

Analysis of the ceramic tiles/EAF slag composite samples (Fig. 3c and d) revealed that the XRD peaks corresponding to the ceramic mixture remained unchanged and retained their original positions. Additionally, new diffraction peaks attributable to EAF slag were observed at their characteristic positions and intensities. This indicates the successful incorporation of the EAF slag filler into the clay matrix of the ceramic tile body. Furthermore, it is clear from Fig. 3c and d that the crystalline structure of the original ceramic tile clay mixture was slightly affected by the addition of EAF slag.

3.1.3. Energy dispersive X-rays (EDX). An EDX analysis was performed on the ceramic tile, EAF slag, ceramic tile with 10.0 wt% EAF slag, and ceramic tile with 40.0 wt% EAF slag. Fig. 4a–d illustrates the results of the overall chemical analysis. As shown in Fig. 4a, the EDX spectrum analysis of the mixture of clays in the ceramic tile specimen confirmed that the sample includes oxygen (O, 57.91% ± 0.15%), silicon (Si, 16.21% ± 0.16%), iron (Fe, 3.20% ± 0.11%), aluminum (Al, 9.15% ± 0.12%), carbon (C, 7.47% ± 0.15%), calcium (Ca, 3.57% ± 0.09%), magnesium (Mg, 0.38% ± 0.03%), sodium (Na, 0.65% ± 0.05%), potassium (K, 0.86% ± 0.04%), and titanium (Ti, 0.62% ± 0.04%). The significant percentage (by mass) of oxygen detected in the ceramic matrix reflects the presence of multiple metal oxides. These oxides are associated with the main constituents of the ceramic matrix, including kaolinite, the primary component of Aswanly clay, quartz, and feldspar. Additionally, calcite and hematite were identified, as detailed in the XRD analysis.

The EDX spectrum and elemental analysis of the EAF slag sample, shown in Fig. 4b, revealed a significant mass percentage of iron (Fe, 15.90% ± 0.29%), oxygen (O, 42.86% ± 0.51%), calcium (Ca, 22.05% ± 0.25%), and silicon (Si, 6.80% ± 0.14%). These elements contribute predominantly to the composition. Additionally, aluminum (Al, 2.98% ± 0.10%), carbon (C, 5.63% ± 0.14%), manganese (Mn, 1.26% ± 0.10%), and magnesium (Mg, 2.51% ± 0.10%) were detected in smaller amounts, along with other trace elements. These findings were further validated by XRD results.

The EDX analysis depicted in Fig. 4c and d illustrate the composition of ceramic tiles that have been incorporated with 10.0 wt% and 40.0 wt% of EAF slag, respectively. The findings indicated the identification of the original peaks typical of ceramic tiles (Fig. 4a), as well as the elemental composition of EAF slag (Fig. 4b), as evidenced by the EDX spectra. This substantiated the inclusion of EAF slag within the ceramic body in specific proportions. The clay mixture in the tile body was only partially replaced by powdered EAF slag. The presence of these elements in a uniform manner across the sample indicates that the EAF slag powder is thoroughly incorporated within the ceramic tile matrix. Moreover, it the intensity of the peaks corresponding to the EAF slag increases proportionally with its wt% in the ceramic tile matrix. This increase in EDX peak intensity further corroborates the successful fabrication of the designed ceramic tile/EAF slag composite materials.

3.1.4. Scanning electron microscope (SEM). Fig. 5a–d present the SEM micrographs of ceramic tile, EAF slag, and the respective samples of ceramic tile combined with EAF slag. The ceramic tile body (Fig. 5a) is composed of an agglomerate of particles that vary in size and exhibit irregular shapes. This structure resembles a rocky film characterized by a rough, less dense morphology and a porous configuration. Such observations have also been reported by Mahmoud *et al.*[51] EAF slag (Fig. 5b) also displays aggregated particles with irregular shapes and a relatively rough surface. The slag particles were sub-rounded to an angular shape with heterogeneous features. The roughness and edges were visible in the bulk and angular particles. Moreover, the SEM analysis of EAF slag indicated that the presence of different mineral phases, such as hematite, wustite, larnite, and magnetite, which vary in both size and shape, is responsible for the rough texture characteristic of the EAF slag surface. The ceramic tiles with 10.0 wt% and 40.0 wt% are depicted in the SEM micrographs shown in Fig. 5c and d. It is evident that the EAF slag is embedded within the clay matrix of the ceramic structure and is uniformly dispersed regardless of the loading level. When incorporating the EAF slag to replace some of the ceramic tile clay mixture, the morphological feature of the ceramic tile body does not change significantly; however, the sample appears to become less porous and possesses a more defined surface morphology and good densification. An increase in the amount of EAF slag results in a more noticeable decline in porosity (illustrated in Fig. 5d). This change contributes to a denser interfacial zone within the ceramic tile/EAF slag composites. Such densification is expected to enhance the gamma-ray shielding capabilities of these materials. Although quantitative image analysis was not performed, the observed reduction in porosity and increased

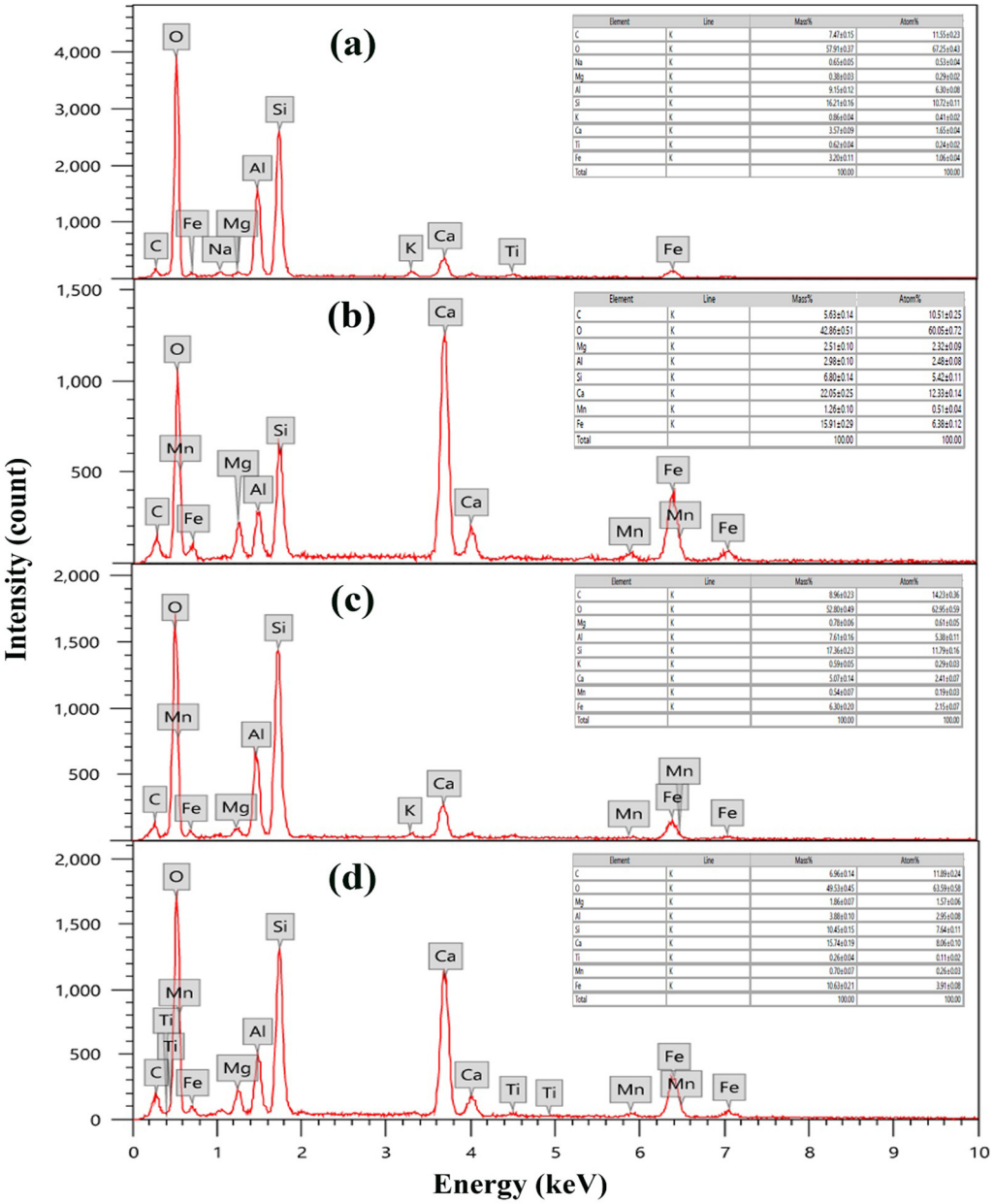

Fig. 4 EDX spectra of (a) standard ceramic tile, (b) electric arc furnace (EAF) steel slag, (c) ceramic tile including 10.0 wt% EAF, and (d) ceramic tile including 40.0 wt% EAF.

packing density in SEM images, along with bulk density and water absorption percentage (AW%) results, serve as reliable indicators of improved densification.

3.2. Physical and mechanical properties

3.2.1. Bending test. This test primarily aims to assess the extent of surface deformation or curvature present in multiple cross-sections of the tested ceramic tile/EAF slag composite materials. The measurements of the deformation of the tile plane along the diagonals and the center line, indicated in millimeters, are summarized in Table 4. It is evident that all tested ceramic tile samples (CT-EAF-0–CT-EAF-4) exhibit minimal deflection from the horizontal plane, ranging from 0.2 mm up to 1.8 mm, remaining within the acceptable range (≤ 2.1).[50] Furthermore, the deviations in linear dimensions and right angles were found to be within permissible tolerance limits defined by the applicable standards, confirming the dimensional stability of the structure. As a result, the incorporation of EAF slag powder within the tile clay matrix did not negatively influence its horizontal plane.

3.2.2. Water absorption percentage (AW%). Water absorption plays a critical role in evaluating the durability of ceramic tile samples. A lower degree of water absorption is typically associated with enhanced durability and improved resistance to environmental factors. The importance of this physical property lies in its direct correlation with the open porosity of

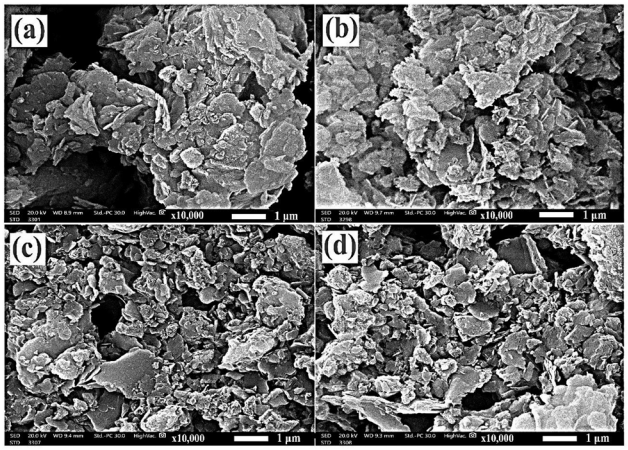

Fig. 5 SEM images of (a) standard ceramic tile, (b) electric arc furnace (EAF) steel slag, (c) ceramic tile including 10.0 wt% EAF, and (d) ceramic tile including 40.0 wt% EAF.

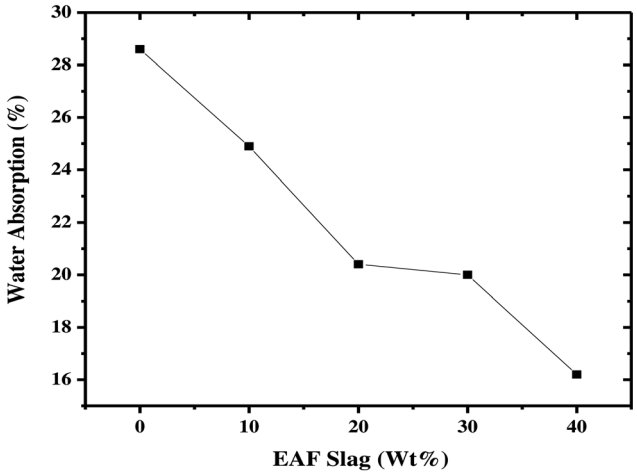

Fig. 6 Percentage of water absorption *versus* EAF slag wt% of the prepared ceramic tiles/EAF slag samples.

the fired ceramic products. Typically, the degree of water absorption (%) is influenced by the amount of filler that is included in the ceramic tile matrix as well as the firing temperature. The data presented in Table 4 and Fig. 6 demonstrate how the EAF slag content (wt%) impacts the AW% of the fabricated ceramic tile/EAF samples. As illustrated in Table 4 and the accompanying curve in Fig. 6, the AW% shows a gradual decrease with increasing EAF slag content in the ceramic tile body. The AW% values decreased from 28.6% for the CT-EAF-0 samples to 16.2% for the CT-EAF-4 samples. The rationale behind this can be attributed to the incorporation of EAF slag as a partial substitute for the clay mixture in the developed ceramic tile composites. Such modification promotes liquid phase sintering during the firing of ceramic tiles, contributing to a denser structure of the tile bodies.[41] An elevation of the EAF slag content from 10.0 wt% to 40.0 wt% would result in higher FeO levels, thereby facilitating the creation of the glassy phase within the ceramic tiles. As a result, the development of a glassy phase during the firing process tends to fill the pores within the ceramic structure. This leads to a reduction in the open porosity of the manufactured tiles. Consequently, the amount of water absorbed by the tiles decreases.[43]

3.2.3. Bulk density (ρ). The bulk densities (ρ) of the tested ceramic tile/EAF slag samples are detailed in Table 3. The data presented in this table clearly indicate a direct relationship between the bulk density of the ceramic tile composite and the weight percentage of EAF slag. The bulk density increases progressively with the rise in the EAF slag content in the tile body. Notably, the CT-EAF-4 sample, containing 40.0 wt% EAF slag, exhibits the highest recorded bulk density of 2.59 $\pm$ 0.77 g cm^{-3}. This increase in density can be attributed to the partial substitution of the raw clay material, particularly quartz powder, in the ceramic tile body with EAF slag. The slag is characterized by its significant iron content and its comparatively higher density of 3.91 g cm^{-3}.

3.2.4. Modulus of rupture (MOR). The data on the average width (b, mm), average thickness (d, mm), average length (x, mm), modulus of rupture (MOR, MPa), and breaking load (F, kg) of ceramic tile samples with EAF slag content ranging from 0.0 to 40.0 wt% is provided in Table 4. The MOR values of the tested ceramic tile/EAF slag samples are plotted in Fig. 7 as a function of the EAF slag wt%. The findings revealed that the strength, as measured by the modulus of rupture (MOR), increased with the addition of EAF slag to the ceramic tile body. The MOR reached its maximum value of 14.0 $\pm$ 0.21 MPa when 20.0 wt% EAF slag was incorporated. A further increase in the EAF slag content resulted in a reduction in MOR, however, the values remained higher than those of the reference ceramic tiles without slag additions (CT-EAF-0). The identified decrease in the MOR result could be a consequence of agglomeration within the sample, particularly when there is a high content of EAF slag in the tile body, as further evidenced by SEM analysis.[43] Generally, the presence of agglomerates predominantly functions

Table 4 Average width (b), average length (x), average thickness (d), the breaking load (F), modulus of rupture (MOR), bending, and water absorption (%) of the prepared ceramic tiles/EAF samples

EAF slag (wt%)	b (mm)	x (mm)	d (mm)	d^2 (mm^2)	F (kg)	MOR MS ISO 10545-4 $\geq$ 1.80 (MPa)	Bending ISO 13006 Spec. $\leq$ 2.1 (mm)	Water absorption (%)
0.0	153.4 $\pm$ 0.1	204.9 $\pm$ 0.1	8.6 $\pm$ 0.01	73.9	37.5 $\pm$ 0.11	5.0 $\pm$ 0.18	0.9–1.0–0.5–0.3	28.6
10.0	154.3 $\pm$ 0.1	205.9 $\pm$ 0.1	8.5 $\pm$ 0.01	72.3	62.3 $\pm$ 0.32	10.0 $\pm$ 0.09	1.0–1.0–1.5–0.6	24.9
20.0	154.4 $\pm$ 0.1	206.1 $\pm$ 0.1	8.7 $\pm$ 0.01	75.7	56.6 $\pm$ 0.40	14.0 $\pm$ 0.21	1.8–1.3–0.9–0.9	20.4
30.0	155.3 $\pm$ 0.1	207.3 $\pm$ 0.1	8.1 $\pm$ 0.01	65.9	26.7 $\pm$ 0.55	7.0 $\pm$ 0.14	0.9–1.2–0.6–0.2	20.0
40.0	155.0 $\pm$ 0.1	207.5 $\pm$ 0.1	7.9 $\pm$ 0.01	62.4	29.7 $\pm$ 0.86	6.0 $\pm$ 0.08	0.8–0.4–0.0–0.5	16.2

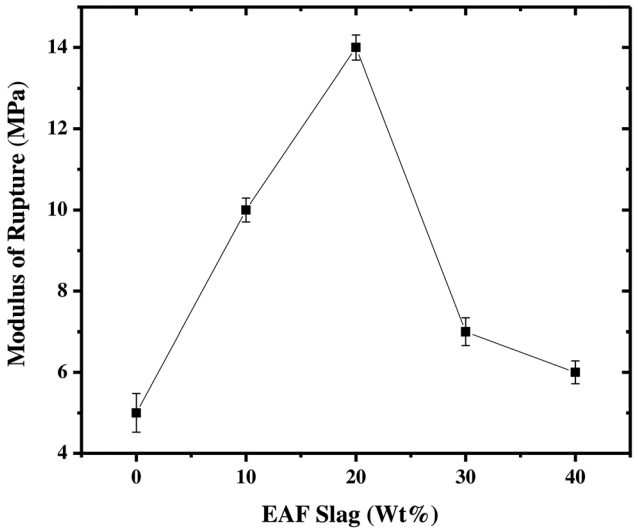

Fig. 7 Values of the modulus of rupture (MPa) *versus* EAF slag wt% of the prepared ceramic tiles/EAF slag samples.

as sites for stress concentration. These sites promote crack initiation within ceramic tiles. Such imperfections are widely recognized as critical weak points that compromise the structural integrity of the tiles.[22] The decline in the MOR value could also result from the uneven dispersion of EAF slag, although this would not be a concern if the steel slag employed had a negligible amount of FeO. Nevertheless, the EAF slag analyzed in this study exhibits an FeO content of around 82.3 wt%. Typically, FeO serves as an effective fluxing agent, and when present in elevated concentration levels, it leads to the generation of an excessive quantity of the glassy phase. The development of such a phase will result in the uneven sealing of the surface pores of the ceramic tiles before the completion of the densification process.[43] The importance of ceramic tiles with enhanced MOR has grown considerably due to the increasing demand for advanced and innovative tile products. Such tiles demonstrate superior properties compared to their parent glass materials. These properties include excellent abrasion resistance, low closed porosity, increased surface hardness, and outstanding chemical resistance.[51]

3.2.5. Micro-hardness. The resistance of a material to surface indentation or penetration under applied pressure can be identified as its hardness.[56] Fig. 8 presents the Vickers hardness (H_v) of the fabricated ceramic tile samples as a function of varying EAF slag wt%, measured under a 300 g load. Upon the application of the indenter, it is evident that the sample has experienced a recoverable elastic pressure. Consequently, the hardness modulus values show an increasing trend in correlation with the rising wt% of EAF slag. This enhancement in hardness is attributed to the binding energy associated with the Fe–O interaction. Thus, the incorporation of EAF slag into the ceramic tile matrix enhances the fine surface hardness of the material. This enhancement contributes to improved gamma radiation resistance and reinforces the mechanical durability of the produced tiles, making them more suitable for long-term shielding applications.[56]

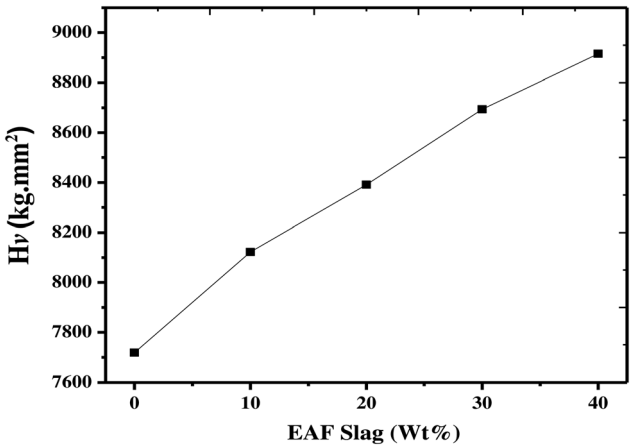

Fig. 8 Variation of Vickers hardness (H_v) with different gamma-ray doses as a function of EAF slag wt%, measured under a 300 g load.

3.3. Gamma-ray shielding properties

Theoretical and experimental analyses were performed on the prepared ceramic tile/EAF slag samples. These analyses aimed to evaluate their gamma-ray shielding effectiveness across various photon energies, including 238, 662, 911, 1173, 1333, and 2614 keV. The extent of penetration of gamma-ray photons into matter is fundamentally governed by μ and μ_m, which are key parameters in understanding this interaction. In Fig. 9, the proportion of gamma-ray photons absorbed per unit thickness of the material is depicted, with 10 wt% EAF serving as a specific case study. The graph illustrates the variation of the natural logarithm of the relative intensity of gamma radiation, $\ln(I/I_0)$, as a function of sample thickness (t, cm) for ceramic tiles containing 10 wt% EAF slag. All data sets in Fig. 9 display a negative linear trend, suggesting that gamma-ray intensity diminishes exponentially as the sample thickness increases. The steepest slope is observed at 238 keV, indicating higher attenuation at a lower photon energy. On the other hand, the slope becomes progressively less steep as the photon energy

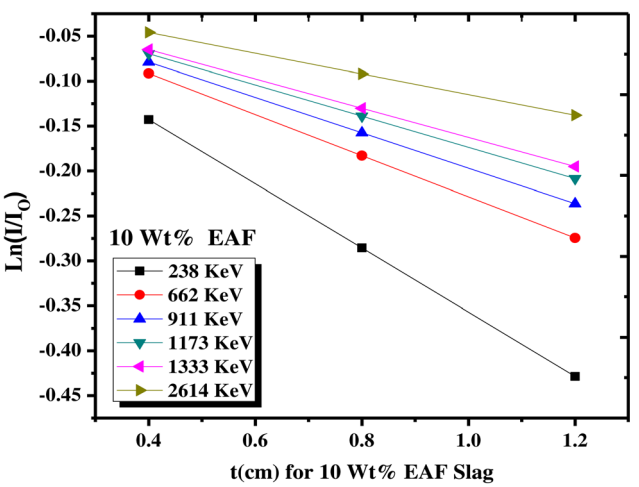

Fig. 9 Linear attenuation coefficients for 10 wt% EAF slag at various photon energies.

increases, with 2614 keV showing the least attenuation. This behavior is attributed to the energy-dependent interaction mechanisms of gamma-rays with matter, where lower-energy photons experience greater attenuation due to higher interaction probabilities. In contrast, higher-energy photons penetrate more deeply and exhibit reduced attenuation, consistent with the established principles of gamma-ray shielding.[17]

Additionally, the μ_m values, derived through theoretical calculations with the WinXCom X-ray computer software, are represented graphically in Fig. 10. From this figure, it is evident that the theoretical values of mass attenuation coefficients increase as the wt% of the EAF slag material in the tile clay matrix rises. This trend is likely attributed to the increasing weight fraction of EAF slag, primarily composed of iron (Fe), a high-Z element with greater bulk density and effective atomic number (Z_{eff}). Its uniform distribution within the tile clay matrix enhances gamma-ray absorption by increasing photon interaction probability, thereby effectively reducing gamma-ray intensity.[22] Moreover, the data shown in Fig. 10 indicate that, across all analyzed curves, the μ_m values are significantly higher at lower photon energies ($E_\gamma < 0.1$ meV) compared to those at higher photon energies ($E_\gamma > 1.022$ meV). The reduction is particularly noticeable when the gamma-ray falls within the range of 1173 to 2614 keV. Such behavior can be interpreted based on the understanding that the mechanisms through which photons interact with matter are determined by the energy region of the photons.[22] Within the lower energy range gamma-rays (less than 400 keV), the photoelectric effect (PE) is the most significant photon–matter interaction mechanism applied. As the energy of the gamma-rays increases, the likelihood of this interaction mechanism decreases, yielding two alternative photon interaction processes: Compton scattering (CS) and pair production (PP).[51] The interaction mechanism of PE is based on energy in the form of $E^{-3.5}$, while CS and PP are based on energy as E^{-1}. This serves to explain why μ_m diminishes rapidly when the photon energy is less than 400 keV.[16] It should be emphasized that at 238 keV, the lowest photon energy, all samples exhibit their maximum μ_m. This is attributed to the fact that the PE is influenced by the atomic number, Z^4–Z^5.[51] As the photon energy of the incoming gamma-rays exceeds this specified level, the $\mu_m(s)$ values for the examined samples become increasingly similar. This can be attributed to the widely recognized trend that a lower interaction probability is observed at higher gamma-ray energies, which is contingent upon the relationship of CS and PP with the atomic number of the shielding material, expressed as Z and Z^2, respectively.[17]

Fig. 11 displays both the experimental and theoretical values of μ_m as a function of the EAF slag wt% at the selected gamma-ray photon energies. The results reveal that the theoretical μ_m values, which were calculated to ensure the validity of the experimental results, show close agreement with the experimental data for the tested samples. This indicates a strong correlation between the measured and calculated outcomes, thereby supporting the reliability of the measured data. The analysis of the data presented in Fig. 11 further confirms that the experimental μ_m values of the ceramic tile/EAF slag composites are significantly influenced by their chemical composition as well as the energy of the incident gamma-rays. Notably, the μ_m values exhibit a marked decrease with increasing gamma-ray photon energy for all ceramic tile samples. Over the energy range of 238 to 2614 keV, μ_m values decrease from 0.1139 to 0.0524 $cm^2\ g^{-1}$ for CT-EAF-0, from 0.1321 to 0.0527 $cm^2\ g^{-1}$ for CT-EAF-1, from 0.1474 to 0.0549 $cm^2\ g^{-1}$ for CT-EAF-2, from 0.1628 to 0.0559 $cm^2\ g^{-1}$ for CT-EAF-3, and from 0.1811 to 0.0563 $cm^2\ g^{-1}$ for CT-EAF-4. These results confirm the inverse relationship between photon energy and gamma-ray attenuation capability. Conversely, at any given photon energy, μ_m values progressively increase with higher EAF slag content in the ceramic tile matrix. This behavior corresponds with the trends previously reported in Fig. 10 and can be explained by the same fundamental mechanisms.[22] At lower energies (<400 keV), the photoelectric effect dominates, which is highly sensitive to the atomic number (proportional to Z^4–Z^5). The substantial FeO content in the slag leads to a significant increase in photoelectric absorption probability. In the intermediate energy region (400–1000 keV), Compton

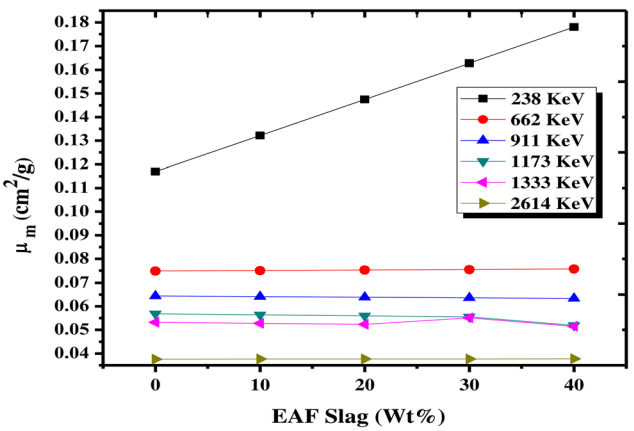

Fig. 10 Theoretical mass attenuation coefficients (μ_m) for various photon energies as a function of EAF slag wt% of the prepared ceramic tiles/EAF slag samples.

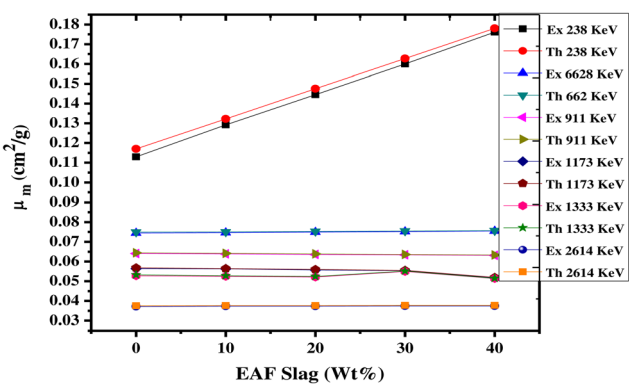

Fig. 11 Experimental and theoretical values of mass attenuation coefficients (μ_m) for various photon energies as a function of EAF slag wt% of the prepared ceramic tiles/EAF slag samples.

scattering, which depends more on electron density than Z, is the prevailing mechanism. The increase in effective electron density (N_{el}) with higher slag content enhances the scattering interaction. At high photon energies (>1.022 meV), pair production becomes relevant, and the increased Fe concentration raises the likelihood of this interaction, as it is proportional to Z^2. Therefore, EAF slag functions not only as a densifying agent but also as an active contributor to the three gamma-ray attenuation mechanisms, owing to its specific elemental composition.

Fig. 12a shows how the HVL values change with the variation of the wt% EAF slag. The observed changes are attributed to variations in the μ_m and the bulk density of the developed ceramic tile/EAF slag samples. It is anticipated that increasing the EAF slag content in the tile body would lead to a reduction in the HVL values. Among the samples analyzed, CT-EAF-0 (ρ = 2.09 ± 0.75 g cm^{-3}) exhibited the highest HVL values (*e.g.*, 2.164 cm at 2614 keV), which can be attributed to its relatively lower density. This observation confirms that gamma-ray photon attenuation at various energies is primarily influenced by the density of the designed material. With an increase in the sample density, the probability of atomic interactions with gamma-ray photons rises, consequently leading to a decrease in the number of photons transmitted through the ceramic tile/EAF slag composites. Thus, the CT-EAF-4 sample, having a density of ρ = 2.59 ± 0.77 g cm^{-3}, exhibited the lowest HVL values (*e.g.*, 0.253 cm at 238 keV). Fig. 12a also illustrates the variation in HVL values related to changes in gamma-ray photon energy. The HVL values were observed to increase as the photon energy increased, indicating that higher-energy photons have greater penetrating ability. This finding is consistent with the results derived from the calculated μ_m values shown in Fig. 11. Thus, it is proposed that samples containing a higher proportion of EAF slag will exhibit superior gamma-ray shielding capabilities, particularly concerning the μ_m and HVL parameters.

In Fig. 12b, it is demonstrated that the behavior of the total electronic cross sections (σ_e) and μ_m, concerning photon energy, is identical. Fig. 12c illustrates that the Z_{eff} values depend on the chemical composition of the tested ceramic tile/EAF slag composite samples. The graph depicts Z_{eff} plotted against varying EAF slag wt% across multiple gamma-ray photon energies. The Z_{eff} values showed a noticeable increase as the EAF slag content in the ceramic tile body increased. The observed enhancement in shielding performance is primarily attributed to the increased bulk density and higher Fe content. These factors enhance both Z_{eff} and μ_m values due to intensified photoelectric absorption, an interaction highly dependent on atomic number, unlike Compton scattering, which is mainly influenced by material density.[16] In composite materials, the

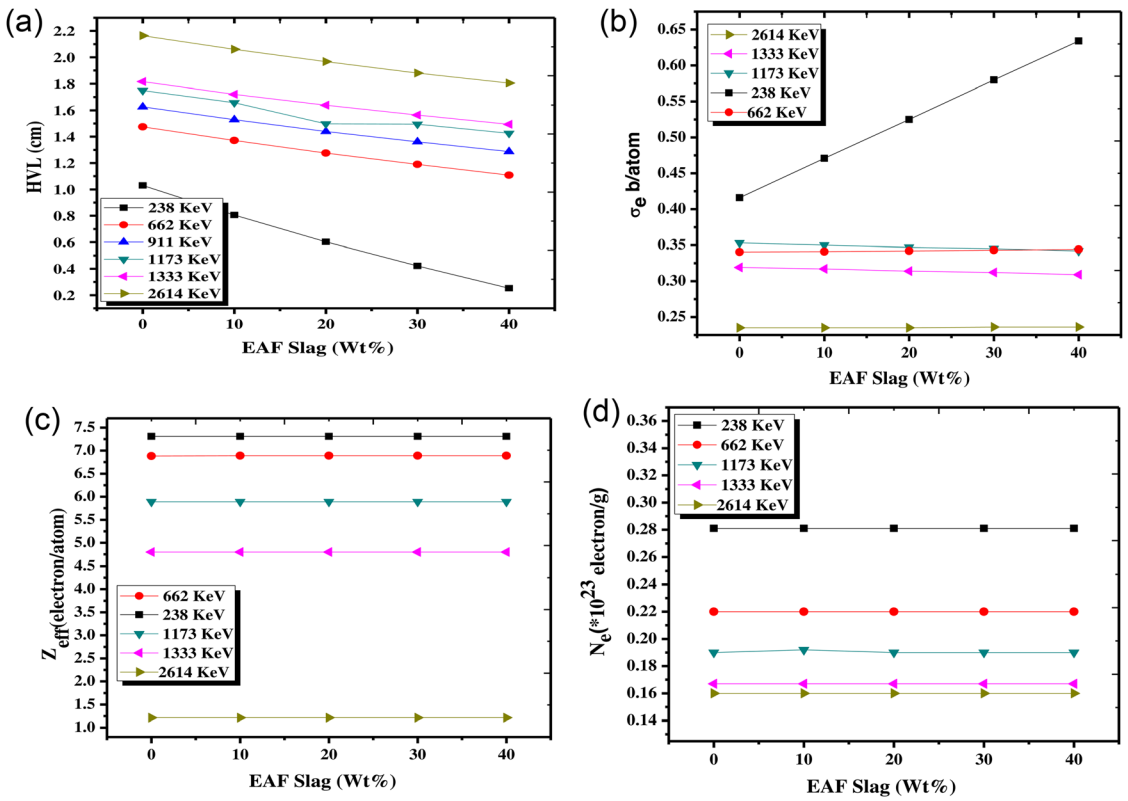

Fig. 12 (a) Variation of HVL as a function of EAF slag wt% of the prepared ceramic tiles/EAF slag samples at different photon energies. (b) Variation of electronic cross section (σ_e) as a function of EAF slag wt% of the prepared ceramic tiles/EAF slag samples at different photon energies. (c) Variation of effective atomic number (Z_{eff}) as a function of EAF slag wt% of the prepared ceramic tiles/EAF slag samples at different photon energies. (d) Variation of effective electron number (N_{el}) as a function of EAF slag wt% of the prepared ceramic tiles/EAF slag samples at different photon energies.

Table 5 Comparison with other previously reported shielding materials at various gamma-ray photon energies

Shielding material	Ref.	Density	Mass attenuation coefficient (μ_m, $cm^2\ g^{-1}$)				Half-value layer (HVL, cm)			
			238 keV	662 keV	1173 keV	1333 keV	238 keV	662 keV	1173 keV	1333 keV
Lead	57	11.34	0.2310 (392 keV)	0.1000	—	0.0560	0.265 (392 keV)	0.611	1.151	1.372
r-PVC	16	1.63	0.1459 (344 keV)	0.0749 (778 keV)	0.0567	0.0393 (1408 keV)	3.193 (392 keV)	5.312 (778 keV)	10.103	14.039
r-PVC + 5.0 wt% Bi_2O_3		1.78	0.1681 (344 keV)	0.0828 (778 keV)	0.0605	0.0448 (1408 keV)	2.844 (392 keV)	4.889 (778 keV)	9.218	11.974
r-PVC + 15.0 wt% Bi_2O_3		1.96	0.2179 (344 keV)	0.1025 (778 keV)	0.0687	0.0520 (1408 keV)	2.356 (392 keV)	4.263 (778 keV)	8.343	10.463
r-PVC + 25.0 wt% Bi_2O_3		2.25	0.2726 (344 keV)	0.1124 (778 keV)	0.0613	0.0710 (1408 keV)	1.973 (392 keV)	3.953 (778 keV)	7.775	9.099
r-PVC + 35.0 wt% Bi_2O_3		2.89	0.3455 (344 keV)	0.1326 (778 keV)	0.0829	0.0753 (1408 keV)	1.629 (392 keV)	3.523 (778 keV)	7.028	7.869
Natural bentonite	58	0.85	—	0.0780	0.0610	0.0560	—	10.023	13.782	14.462
Pressed bentonite (50 bar)		1.04	—	0.0810	0.0620	0.0590	—	8.337	10.008	10.975
Pressed bentonite (100 bar)		1.07	—	0.0820	0.0630	0.0610	—	7.985	9.737	10.193
Pressed bentonite (150 bar)		1.12	—	0.0860	0.0690	0.0650	—	7.111	8.596	9.052
Ceramic tile	22	2.09	0.0781 (356 keV)	0.0697	0.0520	0.0467	4.237 (356 keV)	4.751	6.359	7.087
Ceramic tile containing 2.5 wt% PbO		2.13	0.0852 (356 keV)	0.0751	0.0549	0.0479	3.818 (356 keV)	4.332	5.924	6.788
Ceramic tile containing 5.0 wt% PbO		2.17	0.0988 (356 keV)	0.0840	0.0573	0.0494	3.239 (356 keV)	3.808	5.585	6.478
Ceramic tile containing 7.5 wt% PbO		2.22	0.1204 (356 keV)	0.0898	0.0598	0.0504	2.598 (356 keV)	3.479	5.231	6.211
Ceramic tile containing 10.0 wt% PbO		2.25	0.1327 (356 keV)	0.0968	0.0640	0.0526	2.318 (356 keV)	3.178	4.803	5.849
Unbaked ball clay	59	1.99	—	0.0820 (609 keV)	0.0600	0.0570	—	4.262 (609 keV)	5.794	6.164
Baked ball clay at 1000 °C		1.96	—	0.0821 (609 keV)	0.0601	0.0560	—	4.328 (609 keV)	5.893	6.269
Unbaked kaolin		1.99	—	0.0810 (609.31 keV)	0.0600	0.0570	—	4.273 (609 keV)	5.794	6.164
Baked kaolin at 1000 °C		1.96	—	0.0833 (609 keV)	0.0601	0.0560	—	4.262 (609 keV)	5.785	6.174
Glass composite with chemical formula $60B_2O_3$–$10Bi_2O_3$–15ZnO–$15Na_2O$	60	7.14	0.0070	0.0037	0.0023	0.0023	19.275	36.468 (609 keV)	58.665	58.665
Glass composite with chemical formula $55B_2O_3$–$15Bi_2O_3$–15ZnO–$15Na_2O$		9.26	0.0063	0.0032	0.0019	0.0018	16.479	32.495 (609 keV)	54.7286	57.769
Glass composite with chemical formula $50B_2O_3$–$20Bi_2O_3$–15ZnO–$15Na_2O$		6.26	0.0098	0.0046	0.0026	0.0026	15.705	33.458 (609 keV)	59.195	59.195
Glass composite with chemical formula 45-B_2O_3–$25Bi_2O_3$–15ZnO–$15Na_2O$		7.94	0.0107	0.0039	0.0021	0.0021	11.333	31.095 (609 keV)	57.747	57.747
Concrete	61	2.20	0.1020 (356 keV)	0.0780	0.0580	0.0550	4.286	5.604	7.537	7.947
Volcanic rock		2.80	0.1100 (356 keV)	0.0800	0.0590	0.0560	3.1255	4.297	5.827	6.139
Sandstone		2.60	0.0990 (356 keV)	0.0770	0.0560	0.0530	3.7412	4.810	6.614	6.988
Dolerite		2.55	0.0990 (356 keV)	0.0770	0.0560	0.0540	3.8146	4.905	6.744	6.993
Feldspathic basalt		2.71	0.1010 (356 keV)	0.0780	0.0590	0.0560	3.5183	4.556	6.023	6.346
Compact basalt		2.30	0.0980 (356 keV)	0.0780	0.0590	0.0560	4.272	5.368	7.097	7.476
Pink granite		2.75	0.1100 (356 keV)	0.0800	0.0600	0.0560	3.183	4.3772	5.836	6.253
CT-EAF-0	The present study	2.09	0.1139	0.0749	0.0654	0.0529	1.039	1.475	1.780	1.816
CT-EAF-1		2.20	0.1321	0.0751	0.0681	0.0530	0.806	1.371	1.657	1.720
CT-EAF-2		2.31	0.1474	0.0752	0.0697	0.0552	0.603	1.276	1.561	1.638
CT-EAF-3		2.45	0.1628	0.0754	0.0700	0.0562	0.421	1.191	1.495	1.564
CT-EAF-4		2.59	0.1811	0.0757	0.0707	0.0567	0.253	1.108	1.426	1.499

interactions of gamma-rays and X-rays, including absorption and scattering, are determined by the energy of the photons and the Z_{eff} of the material. Higher Z_{eff} values result in more efficient photon absorption. Accordingly, the ceramic tile sample with 40.0 wt% EAF slag (CT-EAF-4) demonstrated the highest Z_{eff} values (*e.g.*, 7.312 electrons per atom at 238 keV), thereby presenting the greatest probability of interaction with gamma-rays. Fig. 12c also reveals that the Z_{eff} values of the prepared ceramic tile/EAF slag samples decrease with increasing gamma-ray photon energy, exhibiting a nearly continuous trend across varying EAF slag weight percentages at a constant photon energy. This behavior is attributed to the same mechanisms discussed previously, primarily the reduced contribution of photoelectric absorption at higher photon energies.[22]

The N_{el} values for the examined ceramic tile/EAF slag composites were calculated based on the μ_m results[22] in the photon energy range of 238–2614 keV, as shown in Fig. 12d. The variation in N_{el} followed a trend similar to that of Z_{eff} for the investigated samples (CT-EAF-0 up to CT-EAF-4), decreasing as the gamma-ray photon energy increased. However, the N_{el} values increased progressively with higher EAF slag content in the tile body, indicating enhanced photon interaction capability due to the greater presence of high-Z elements. Generally, the variation in N_{el} for compounds and mixtures is governed by Z_{eff}, as the effective atomic number is directly related to the number of electrons in the constituent elements, which in turn influences the interaction of the material with incident photons. Additionally, the results regarding different EAF slag weight fractions show only slight discrepancies; a higher N_{el} value would suggest an enhanced probability of energy deposition and photon–electron energy transfer within the samples.[17]

Finally, to assess the performance of the developed ceramic tiles/EAF slag composites, the measured μ_m as well as HVL values were compared against the values of various materials that had been previously evaluated for shielding applications at 238, 662, 1173, and 1333 keV, as summarized in Table 5. The data collected in this study reveal that the designed composites offer gamma-ray shielding characteristics that are comparable to, or even potentially exceed, those reported in earlier investigations. The effective gamma-ray absorption observed is a direct consequence of the uniformity in the dispersion of EAF, which possesses a high atomic number, high density, and a considerable Z_{eff}. The tested composites can additionally be regarded as a sustainable and durable material, characterized by a ceramic tile clay matrix that displays favorable gamma-ray photon absorption capabilities over a wide range of photon energies and at low thickness. The developed ceramic tile materials, owing to their enhanced gamma-ray shielding properties, can be effectively utilized in a variety of radiation protection applications. These include the nuclear industry, medical imaging and oncology departments in hospitals, radiation therapy facilities, nuclear power plants, radioactive waste storage sites, and radiation research laboratories. Its structural integrity and shielding efficiency also make it suitable for protective wall linings, floors, and enclosures in environments with high levels of ionizing radiation.

4. Conclusion

In summary, this study investigated the use of EAF slag as a sustainable additive (up to 40 wt%) in standard ceramic tiles to enhance their gamma-ray shielding performance in nuclear environments. The characteristics related to the physical, structural, mechanical, and gamma-ray shielding of the prepared ceramic tile/EAF slag were analyzed. FTIR and SEM analyses confirmed strong interaction and uniform dispersion of EAF slag in the ceramic matrix, while XRD analysis identified a composite structure with both crystalline and amorphous phases. The bulk density values were found to increase with higher EAF slag content (from 2.20 ± 0.68 to 2.59 ± 0.77 g cm^{-3}), enhancing material compactness. In addition, the mechanical properties of the ceramic tile/EAF slag composites, including MOR and H_v, were improved, peaking at 20.0 wt% EAF slag (14.0 ± 0.21 MPa) for MOR and continuously increasing for H_v. The gamma-ray shielding performance of the ceramic tile/EAF slag composites improved significantly with increasing EAF slag content in the tile body, particularly at 40.0 wt%. This enhancement is evidenced by increased values of the μ_m, Z_{eff}, and N_{el}, along with a corresponding reduction in the HVL, indicating superior shielding efficiency. Also, experimental shielding results were found to align well with the theoretical predictions using WinXCOM. These outcomes reveal the strong potential of EAF slag-infused ceramic tiles as high-performance materials for gamma-ray shielding, particularly in nuclear infrastructure. However, future research studies are suggested to study and address long-term durability under environmental stressors, such as humidity and thermal cycling, to validate their suitability for real-world radiation shielding conditions.

Conflicts of interest

There are no conflicts to declare.

Data availability

All data underlying the results are available as part of the article, and no additional source data are required.

Acknowledgements

This research has been funded by the Scientific Research Deanship at the University of Hail, Saudi Arabia, through project number (RG-23153).

References

1 V. J. Gonzalez, C. R. Hullett, L. Burt, P. Rassiah-Szegedi, V. Sarkar, J. D. Tward, L. J. Hazard, Y. J. Huang, B. J. Salter and D. K. Gaffney, Impact of prone versus supine positioning on small bowel dose with pelvic intensity modulated radiation therapy, *Adv. Radiat. Oncol.*, 2017, **2**, 235–243.
2 Y. Kavun, I. Boztosun, H. Dapo, I. Maraş and C. Segebade, Determination of the Sr/Ca ratio of tooth samples by

photoactivation analysis in Southern Turkey, *Radiochim. Acta*, 2018, **106**, 759–768.
3 A. Kahraman and E. Yilmaz, Irradiation response of radio-frequency sputtered Al/Gd_2O_3/p-Si MOS capacitors, *Radiat. Phys. Chem.*, 2017, **139**, 114–119.
4 X. B. Wang, C. N. Wang, Y. C. Zhang, T. T. Liu, J. P. Lv, X. Shen and M. R. Guo, Effects of gamma radiation on microbial, physicochemical, and structural properties of whey protein model system, *J. Dairy Sci.*, 2018, **101**, 4879–4890.
5 S. Harris, M. D. Chan, J. F. Lovato, T. L. Ellis, S. B. Tatter, J. D. Bourland, M. T. Munley, A. F. deGuzman, E. G. Shaw, J. J. Urbanic and K. P. McMullen, Gamma knife stereotactic radiosurgery as salvage therapy after failure of whole-brain radiotherapy in patients with small-cell lung cancer, *Int. J. Radiat. Oncol., Biol., Phys.*, 2012, **83**, e53-9.
6 National Research Council, *Health Risks from Exposure to Low Levels of Ionizing Radiation: BEIR VII Phase 2*, The National Academies Press, Washington, DC, 2006.
7 P. Vaz, Radiological protection, safety and security issues in the industrial and medical applications of radiation sources, *Radiat. Phys. Chem.*, 2015, **116**, 48–55.
8 G. Hu, H. Hu, Q. Yang, B. Yu and W. Sun, Study on the design and experimental verification of multilayer radiation shield against mixed neutrons and γ-rays, *Nucl. Eng. Technol.*, 2020, **52**, 178–184.
9 A. El-Taher, A. M. Ali, Y. B. Saddeek, R. Elsaman, H. Algarni, Kh. S. Shaaban and T. Z. Amer, Gamma ray shielding and structural properties of iron alkali alumino-phosphate glasses modified by PbO, *Radiat. Phys. Chem.*, 2019, **165**, 108403.
10 L. A. Najam, A. K. Hashim, H. A. Ahmed and I. M. Hassan, Study the Attenuation Coefficient of Granite to Use It as Shields against Gamma Ray, *Detection*, 2016, **4**, 33–39.
11 B. Aygün, High alloyed new stainless steel shielding material for gamma and fast neutron radiation, *Nucl. Eng. Technol.*, 2020, **52**, 647–653.
12 Y. B. Saddeek, K. H. S. Shaaban, R. Elsaman, A. El-Taher and T. Z. Amer, Attenuation-density anomalous relationship of lead alkali borosilicate Glasses, *Radiat. Phys. Chem.*, 2018, **150**, 182–188.
13 S. S. Obaid, D. K. Gaikwad and P. P. Pawar, Determination of gamma ray shielding parameters of rocks and concrete, *Radiat. Phys. Chem.*, 2018, **144**, 356–360.
14 G. M. Barrera, J. J. del Coz-Díaz, E. M. Cruz, M. M. López, M. C. S. Ribeiro, C. V. Santos, H. E. H. Lobland and W. Brostow, Modified recycled tire fibers by gamma radiation and their use on the improvement of polymer concrete, *Constr. Build. Mater.*, 2019, **204**, 327–334.
15 K. S. Mann, A. Rani and M. S. Heer, Shielding behaviors of some polymer and plastic materials for gamma-rays, *Radiat. Phys. Chem.*, 2015, **106**, 247–254.
16 R. M. El-Sharkawy, F. S. Abdou, M. A. Gizawy, E. A. Allam and M. E. Mahmoud, Bismuth oxide nanoparticles (Bi_2O_3 NPs) embedded into recycled- Poly(vinyl chloride) plastic sheets as a promising shielding material for gamma radiation, *Radiat. Phys. Chem.*, 2023, **208**, 110838.
17 R. M. El-Sharkawy, E. A. Allam, A. El-Taher, R. Elsaman, E. El Sayed Massoud and M. E. Mahmoud, Synergistic effects on gamma-ray shielding by novel light-weight nanocomposite materials of bentonite containing nano Bi_2O_3 additive, *Ceram. Int.*, 2022, **48**, 7291–7303.
18 R. N. Ihsani, P. L. Gareso and D. Tahir, An overview of gamma radiation shielding: Enhancements through polymer-lead (Pb) composite materials, *Radiat. Phys. Chem.*, 2024, **218**, 111619.
19 R. Ji, Z. Zhang, C. Yan, M. Zhu and Z. Li, Preparation of novel ceramic tiles with high Al_2O_3 content derived from coal fly ash, *Constr. Build. Mater.*, 2016, **114**, 888–895.
20 O. Turkmen, A. Kucuk and S. Akpinar, Effect of wollastonite addition on sintering of hard porcelain, *Ceram. Int.*, 2015, **41**, 5505–5512.
21 M. F. Serra, M. S. Conconi, G. Suarez, E. F. Aglietti and N. M. Rendtorff, Volcanic ash as flux in clay-based triaxial ceramic materials, effect of the firing temperature in phases and mechanical properties, *Ceram. Int.*, 2015, **41**, 6169–6177.
22 M. E. Mahmoud, A. M. El-Khatib, A. M. Halbas and R. M. El-Sharkawy, Investigation of physical, mechanical, and gamma-ray shielding properties using ceramic tiles incorporated with powdered lead oxide, *Ceram. Int.*, 2020, **46**, 15686–15694.
23 B. Oto, E. Kavaz, H. Durak, A. Aras and Z. Madak, Effect of addition of molybdenum on photon and fast neutron radiation shielding properties in ceramics, *Ceram. Int.*, 2019, **45**, 23681–23689.
24 F. Akman, Z. Y. Khattari, M. R. Kaçal, M. I. Sayyed and F. Afaneh, The radiation shielding features for some silicide, boride and oxide types ceramics, *Radiat. Phys. Chem.*, 2019, **160**, 9–14.
25 V. P. Singh, N. M. Badiger and T. Korkut, Gamma exposure buildup factors and neutron total cross section of ceramic hosts for high-level radioactive wastes, *Prog. Nucl. Energy*, 2018, **104**, 1–7.
26 M. R. Kacal, F. Akman and M. I. Sayyed, Investigation of radiation shielding properties for some ceramics, *Radiochim. Acta*, 2019, **107**, 179–191.
27 A. A. Jawad, N. Demirkol, K. Gunoğlu and I. Akkurt, Radiation shielding properties of some ceramic waste samples, *Int. J. Environ. Sci. Technol.*, 2019, **16**, 5039–5042.
28 A. Ripin, F. Mohamed, T. F. Choo, M. R. Yusof, S. Hashim and S. K. Ghoshal, X-ray shielding behaviour of kaolin-derived mullite-barites ceramic, *Radiat. Phys. Chem.*, 2018, **144**, 63–68.
29 T. Özdemir and S. N. Yılmaz, Hexagonal boron nitride and polydimethylsiloxane: a ceramic rubber composite material for neutron shielding, *Radiat. Phys. Chem.*, 2018, **152**, 93–99.
30 Y. Ke, Y. Chen, S. Liang, J. Hu, H. Hou, J. Quan, X. Li, H. Duan, S. Yuan and J. Yang, Environmentally sound management of industrial solid waste: A paradigm of proposed bi-tetrahedron, *Resour., Conserv. Recycl.*, 2023, **198**, 107212.
31 R. Li, Y. Zhou, C. Li, S. Li and Z. Huang, Recycling of industrial waste iron tailings in porous bricks with low thermal conductivity, *Constr. Build. Mater.*, 2019, **213**, 43–50.

32 P. V. Nidheesh and M. S. Kumar, An overview of environmental sustainability in cement and steel production, *J. Clean. Prod.*, 2019, **231**, 56–871.
33 J. Choudhary, B. Kumar and A. Gupta, Utilization of solid waste materials as alternative fillers in asphalt mixes: A review, *Constr. Build. Mater.*, 2020, **234**, 117271.
34 J. Feng, J. Yang, S. Cui, K. Hu, F. Wang, P. Ning and L. Jia, Waste to wealth: Efficient wet desulfurization of electric arc furnace dust (EAFD) and recycling of desulfurization solid residue, *Chem. Eng. J.*, 2024, **491**, 152053.
35 M. Awaad, S. M. Naga and N. El-Mehalawy, Effect of replacing weathered feldspar with potash feldspar in the production of stoneware tiles containing fish bone ash, *Ceram. Int.*, 2015, **41**, 7816–7822.
36 P. T. Teo, A. S. Anasyida, C. M. Kho and M. S. Nurulakmal, Recycling of Malaysia's EAF steel slag waste as novel fluxing agent in green ceramic tile production: Sintering mechanism and leaching assessment, *J. Clean. Prod.*, 2019, **241**, 118144.
37 C. Mourou, M. Zamorano, D. P. Ruiz and M. M. Morales, Characterization of ceramic tiles coated with recycled waste glass particles to be used for cool roof applications, *Constr. Build. Mater.*, 2023, **398**, 132489.
38 F. Faleschini, K. Brunelli, M. A. Zanini, M. Dabalà and C. Pellegrino, Electric Arc furnace as coarse recycled aggregate for concrete production, *J. Sustainable Metall.*, 2016, **2**, 44–50.
39 A. S. Ouda and H. A. Abdel-Gawwad, The effect of replacing sand by iron slag on physical, mechanical and radiological properties of cement mortar, *HBRC J.*, 2017, **13**, 255–261.
40 H. Chen, Y. Liu, H. Cui, W. Zhang, L. Hu and L. Mao, Effects of electric arc furnace slag on promoting quality and environmental safety of fired bricks incorporating municipal solid waste incineration fly ash, *Constr. Build. Mater.*, 2022, **345**, 128327.
41 P. T. Teo, A. S. Anasyida, P. Basu and M. S. Nurulakmal, Recycling of Malaysia's electric arc furnace (EAF) slag waste into heavy-duty green ceramic tile, *Waste Manage.*, 2014, **34**, 2697–2708.
42 R. Sarkar, N. Singh and S. Kumar, Utilization of steel melting electric arc furnace slag for development of vitreous ceramic tiles, *Bull. Mater. Sci.*, 2010, **33**, 293–298.
43 H. Badiee, A. Maghsoudipour and B. R. Dehkordi, Use of Iranian steel slag for production of ceramic floor tiles, *Adv. Appl. Ceram.*, 2008, **107**, 111–115.
44 A. M. Ibrahim, A. R. Mohamed, A. M. El-Khatib, M. T. Alabsy and M. Elsalamawy, Effect of hematite and iron slag as aggregate replacement on thermal, mechanical, and gamma-radiation shielding properties of concrete, *Constr. Build. Mater.*, 2021, **310**, 125225.
45 B. Pomaro, F. Gramegna, R. Cherubini, V. De Nadal, V. Salomoni and F. Faleschini, Gamma-ray shielding properties of heavyweight concrete with Electric Arc Furnace slag as aggregate: an experimental and numerical study, *Constr. Build. Mater.*, 2019, **200**, 188–197.
46 M. Maslehuddin, A. A. Naqvi, M. Ibrahim and Z. Kalakada, Radiation shielding properties of concrete with electric arc furnace slag aggregates and steel shots, *Ann. Nucl. Energy*, 2013, **53**, 192–196.
47 S. Özen, C. Şengül, T. Erenoğlu, Ü. Çolak, İ. A. Reyhancan and M. A. Taşdemir, Properties of heavyweight concrete for structural and radiation shielding purposes, *Arab J. Sci. Eng.*, 2016, **41**, 1573–1584.
48 ASTM C373-88, Standard Test Method for Water Absorption, Bulk Density, Apparent Porosity, and Apparent Specific Gravity of Fired Whiteware Products, 02, Glass Ceramics, 2006.
49 BS EN ISO 10545-4, Ceramic Tiles. Part 4. Determination of Modulus of Rupture and Breaking Strength, 1995.
50 International Organization for Standardization, ISO 13006: Ceramic Tiles – Definitions, Classification, Characteristics and Marking, 1998.
51 M. E. Mahmoud, A. M. El-Khatib, A. M. Halbas and R. M. El-Sharkawy, Ceramic tiles doped with lead oxide nanoparticles: Their fabrication, physical, mechanical characteristics and γ-ray shielding performance, *Radiat. Phys. Chem.*, 2021, **189**, 109780.
52 Z. M. Wang, J. G. Li, B. Liu, Y. N. Zeng and Z. Y. Gao, Study on mineralogical phase composition and quantitative analysis of argon oxygen decarburization slag, *Metall. Anal.*, 2017, **37**, 15–20.
53 N. E. Menad, N. Kana, A. Seron and N. Kanari, New EAF Slag Characterization Methodology for Strategic Metal Recovery, *Mater.*, 2021, **14**, 1513.
54 N. Kanari, E. Allain, L. Filippov, S. Shallari, F. Diot and F. Patisson, Reactivity of Low-Grade Chromite Concentrates towards Chlorinating Atmospheres, *Mater.*, 2020, **13**, 4470.
55 U.S. Environmental Protection Agency (USEPA), (1992). Method 1311: Toxicity Characteristic Leaching Procedure. Test Methods for Evaluating Solid Waste, Physical/Chemical Methods (SW-846).
56 J. Luo, H. Wang, C. Xi, H. Zhai, Y. Gu and C. Zhang, Indentation size effect–crack propagation model and finite element simulation verification for microhardness test of ceramic materials, *Ceram. Int.*, 2021, **47**, 4914–4924.
57 E. E. Belgin and G. A. Aycik, Preparation and radiation attenuation performances of metal oxide filled polyethylene based composites for ionizing electromagnetic radiation shielding applications, *J. Radioanal. Nucl. Chem.*, 2015, **306**, 107117.
58 I. Z. Hager, Y. S. Rammah, H. A. Othman, E. M. Ibrahim, S. F. Hassan and F. H. Sallam, Nano-structured natural bentonite clay coated by polyvinyl alcohol polymer for gamma rays attenuation, *J. Theor. Appl. Phys.*, 2019, **13**, 141–153.
59 S. F. Olukotun, S. T. Gbenu, F. I. Ibitoye, O. F. Oladejo, H. O. Shittu, M. K. Fasasi and F. A. Balogun, Investigation of gamma radiation shielding capability of two clay materials, *Nucl. Eng. Technol.*, 2018, **50**, 957–962.
60 A. H. Ghanem, A. T. M. Farag, A. G. Al-Sehemi, A. Al-Ghamdi, W. A. Farooq and F. Yakuphanoglu, Bismuth borate glass-based nuclear materials, *Silicon*, 2018, **10**, 1195–1201.
61 S. S. Obaid, D. K. Gaikwad and P. P. Pawar, Determination of gamma ray shielding parameters of rocks and concrete, *Radiat. Phys. Chem.*, 2018, **144**, 356–360.